Featured in Physics

Asymmetry Control in a Parametric Oscillator for the Quantum Simulation of Chemical Activation

Alejandro Cros Carrillo de Albornoz,[1,2,*,†] Rodrigo G. Cortiñas,[1,*,‡,§] Max Schäfer,[1,*,‖,¶] Nicholas E. Frattini,[1,**] Brandon Allen,[3] Delmar G.A. Cabral,[3] Pablo E. Videla,[3] Pouya Khazaei,[4] Eitan Geva,[4] Victor S. Batista,[3] and Michel H. Devoret[1,††,‡‡]

[1] *Department of Applied Physics and Physics, Yale University, New Haven, Connecticut 06520, USA*
[2] *Department of Physics and Astronomy, University College London, London WC1E 6BT, United Kingdom*
[3] *Department of Chemistry, Yale University, New Haven, Connecticut 06520, USA*
[4] *Department of Chemistry, University of Michigan, Ann Arbor, Michigan 48109, USA*

(Received 8 May 2025; revised 22 January 2026; accepted 25 February 2026; published 16 April 2026)

Dissipative tunneling remains a cornerstone effect in quantum mechanics. In chemistry, it plays a crucial role in governing the rates of chemical reactions, often modeled as the motion along the reaction coordinate from one potential well to another. The relative positions of energy levels in these wells strongly influence the reaction dynamics. Chemical research will benefit from a fully adjustable, asymmetric double-well equipped with precise measurement capabilities of the tunneling rates. In this paper, we show a quantum simulator system that consists of a continuously driven Kerr parametric oscillator with a third-order nonlinearity that can be operated in the quantum regime to create a fully tunable asymmetric double-well. Our experiment leverages a low-noise, all-microwave control system with a high-efficiency readout, based on a tunnel Josephson junction circuit, of the which-well information. We explore the reaction rates across the landscape of tunneling resonances in parameter space. We uncover two counter-intuitive effects: (i) a weak asymmetry can significantly decrease the activation rates, even though the well in which the system is initialized is made shallower, and (ii) the width of the tunneling resonances alternates between narrow and broad lines as a function of the well depth and asymmetry. We predict by numerical simulations that both effects will also manifest themselves in ordinary chemical double-well systems in the quantum regime. Our work is a first step for the development of analog molecule simulators of proton transfer reactions based on quantum parametric processes.

DOI: 10.1103/71yp-fqns

I. INTRODUCTION

Engineering Hamiltonians to produce a desired potential landscape is a crucial task in quantum computing [1–6]. Among these landscapes, double-wells hold particular importance, serving as models for diverse systems like two-level defects [7,8], nuclear structures [9], and chemical reactions [6,10]. However, tuning parameters experimentally within these systems, like the barrier height, often proves to be challenging [6,11]. Additionally, classical computational models can struggle with accuracy, e.g., failing to reach chemical accuracy [12]. Consequently, developing a low-noise system capable of generating tunable double-well potentials is highly desirable for the simulation of quantum chemistry problems.

In this paper, we report the results of the activation dynamics of a continuously tunable asymmetric double-well parametric oscillator suitable for the simulation of chemical activation. During our exploration, we found two unexpected effects. First, we find that the asymmetric double-well can experience a significantly

*These authors contributed equally to this work.
†Contact author: a.croscarrillo@gmail.com
‡Present address: Google Quantum AI, Santa Barbara, CA, USA.
§Contact author: rodrigogc@google.com
‖Present address: Department of Physics, University of California, Santa Barbara, CA, USA.
¶Contact author: maxschaefer@ucsb.edu
**Present address: Nord Quantique, Sherbrooke, QC J1J 2E2, Canada.
††Present addresses: Google Quantum AI, Santa Barbara, CA, USA and Department of Physics, University of California, Santa Barbara, CA, USA.
‡‡Contact author: devoret@ucsb.edu

longer activation time (well-switching time) from one well to the other than the symmetric one, even when the system is initialized in the shallower well. This is counterintuitive because one would think that by reducing the barrier height, the activation time should decrease [13–15]. We find this is not always the case in our system due to a subtle quantum effect described below. This suggests an unexpected technique to stabilize bosonic quantum states. The second unexpected effect is that the activation exhibits pronounced quantum resonances whose width alternates between narrow and broad with both the depth and the asymmetry of the wells. This is a manifestation of the width of the Hamiltonian anticrossing of the energy levels close to the top of the barrier of the double-well energy surface. The location and width of these resonances are well explained by a Hamiltonian model within the rotating wave approximation (RWA) and by a semiclassical model.

Based on the experimental and theoretical observation of these effects in the Kerr parametric oscillator (KPO), we investigate whether they can be generalized to other double-well systems and assess the capacity of our system to deal with quantum simulation applications. A particularly important class of double-well problems is found in chemistry for modeling electron-transfer reactions [6] and proton tunneling [16]. We predict the effects should be generically observable in quantum dissipative double-wells, in particular also in double-wells that are used to model transfer reactions like between the guanine-cytosine DNA base pairs. Finally, we point out that the results reported in this paper lead to the proposal that our implementation can be tuned, within realistic parameters, to quantum simulate precisely these [16].

II. SETUP AND MODEL SYSTEM

Our setup was first described in [17], with the current implementation first introduced in [18] and summarized here for the sake of completeness. The sample consists of two chips with superconducting circuits, shown in Fig. 1(a), that are addressable by microwave drives via charge-coupling. In this experiment, we only make use of one of the two chips, but we note that applications based on multiple devices are within the range of present-day technology (see Sec. IV). The relevant chip contains an array of two superconducting nonlinear asymmetric inductive elements (SNAILs) [19,20] shunted by a large capacitor [17], as depicted in Figs. 1(b)–1(d). We include a wiring diagram of the setup in Appendixes.

The Hamiltonian of our SNAIL transmon with charge drives can be approximated as [17,20]

$$\frac{\hat{H}(t)}{\hbar} = \omega_o \hat{a}^\dagger \hat{a} + \frac{g_3}{3}(\hat{a}+\hat{a}^\dagger)^3 + \frac{g_4}{4}(\hat{a}+\hat{a}^\dagger)^4 - i\Omega_1 \sin(\omega_1 t + \phi)(\hat{a}-\hat{a}^\dagger) - i\Omega_2 \sin(\omega_2 t)(\hat{a}-\hat{a}^\dagger), \quad (1)$$

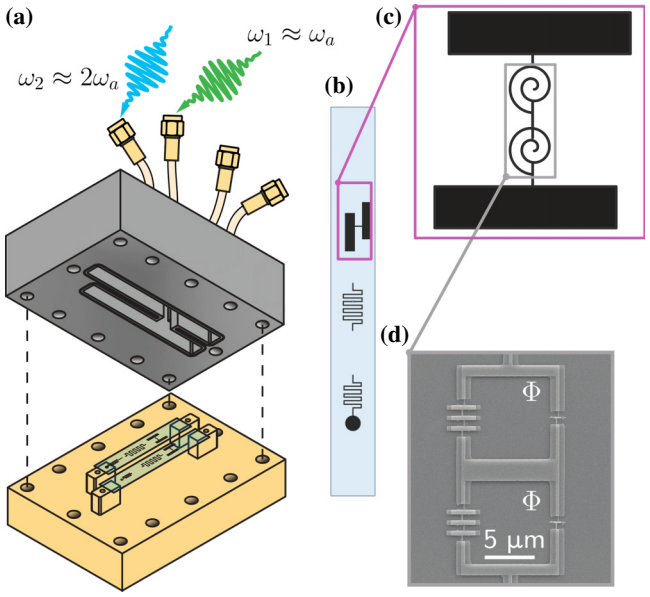

FIG. 1. Experimental setup. (a) Rendering of the half-aluminum, half-copper sample package containing two sapphire chips magnified in (b). Each chip consists of a SNAIL transmon, a readout resonator, and a Purcell filter. Only one chip is used in this work. The normalized resonance frequency of the SNAIL transmon is denoted ω_a. Applying a strong microwave drive at $\omega_2 \approx 2\omega_a$ morphs the SNAIL-transmon Hamiltonian into the parametric oscillator Hamiltonian. (c) Schematic of the SNAIL transmon: a two-SNAIL array serves as the nonlinear element. The capacitor pads are shifted with respect to the axis of the array to couple it to the readout resonator. (d) Scanning electron micrograph of the two-SNAIL arrays. The SNAIL loops are biased with an external magnetic flux $\Phi/\Phi_0 = 0.31$, where Φ_0 is the magnetic flux quantum. Figure adapted from [18].

where ω_o is the bare resonance frequency of the SNAIL transmon, g_3, g_4 are the third- and fourth-order nonlinearities of the circuit, and $\hat{a}$ is the bosonic annihilation operator. This Hamiltonian is the so-called (asymmetric) parametric oscillator Hamiltonian when $\omega_2 \approx 2\omega_o$ and $\omega_1 = \omega_2/2$ [21,22]. Here, Ω_1 is the amplitude and ω_1 is the frequency of the one-photon drive that will henceforth be referred to as the linear, or additive, drive, while Ω_2 and ω_2 are the amplitude and frequency of what we refer to as the squeezing, or two-photon, parametric drive. The phase ϕ is the relative phase between the two drives.

By applying displaced frame transformations, transforming into the rotating frame at $\omega_2/2$ and keeping some terms beyond the RWA [18,23], we arrive at the effective Hamiltonian describing the asymmetric parametric oscillator

$$\frac{\hat{H}_{\text{eff}}}{\hbar} = \Delta \hat{a}^\dagger \hat{a} - K \hat{a}^{\dagger 2} \hat{a}^2 + \epsilon_2 \hat{a}^2 + \epsilon_1 e^{i\phi} \hat{a} + \text{H.c.} \quad (2)$$

where $\Delta = \omega_2/2 - \omega_a$ is the detuning, $\omega_a \approx \omega_o$ the renormalized SNAIL transmon resonance frequency, and $K = -(3g_4/2) + (10g_3^2/3\omega_a)$ is the leading-order Kerr nonlinearity. The drive coefficients are given by $\epsilon_1 = (\Omega_1/2)$ and $\epsilon_2 = g_3(4\Omega_2/3\omega_a)$. The relation to a double-well becomes apparent in the classical limit by defining

$$\frac{V(x)}{\hbar} = \frac{H_{\text{eff}}}{\hbar}\bigg|_{p=0} = k_4x^4 - k_2x^2 + k_1x, \tag{3}$$

where $\hat{a} \mapsto (1/\sqrt{2})(x + ip)$ together with $k_1 = \sqrt{2}\epsilon_1 \cos\phi$, $k_2 = -(\epsilon_2 + \Delta/2)$, and $k_4 = -K/4$. Two instances of $V(x)$ are shown in Figs. 2(a) and 2(c), while in Figs. 2(b) and 2(d), the associated energy spectra of Eq. (2) are shown as a function of the control parameters ϵ_1 and ϵ_2 for $\phi = 0$. From Eq. (2) or (3), ϵ_1 controls the asymmetry of the wells and ϵ_2 controls their depth [21]. Note, however, that the parametric oscillator Hamiltonian cannot be written as a sum of kinetic $[T(p)]$ and potential $[V(x)]$ energy since cross-terms like x^2p^2 are present. These terms can lead to interesting consequences [14,24–26]. However, the perturbation of the energy levels due to these cross-terms can be decreased by reducing the zero-point spread of the oscillator. We show a rigorous derivation of the perturbative nature of these terms, as well as their impact on the simulation of chemistry, in [16]. The perturbations due to cross-terms do not play a critical role in the new effects described in this paper, as shown by the fact that a prototypical chemical double-well Hamiltonian without such cross-terms displays the same effects as the KPO (see Sec. IV).

For $\epsilon_1 = 0$, we recover the conventional (symmetric) parametric oscillator Hamiltonian that creates a double-well along the position axis [17,18,25–28]. If $\epsilon_1 \neq 0$, the phase ϕ becomes relevant. For $\phi = 90°$, the linear drive adds a term proportional to the "momentum," p, thus not breaking the symmetry between the wells. For $\phi = 0$, this drive adds a term proportional to the "position," x, thus lifting the degeneracy between the two wells [21,29] [see Figs. 2(c) and 2(d)]. In the main text, we focus on the case $\phi = 0$ and leave the experimental study of the effect of the phase variation for Appendixes.

To model the activation rate, we use an ordinary Lindbladian model containing only single-photon gain and single-photon loss with phenomenological rates and temperature [27,30,31] that we directly fit to our data.

III. EXPERIMENT AND ANALYSIS

To ready the setup for our experiments, we bias our SNAIL loops with an external magnetic field sourced by a solenoid lying below the copper part of the enclosure [orange block in Fig. 1(a)]. This flux sets the frequency ω_a and the Kerr nonlinearity K. For the theory plots in Figs. 4 and 5, we fit $\Delta/2\pi = 558$ kHz and $K/2\pi = 465$ kHz

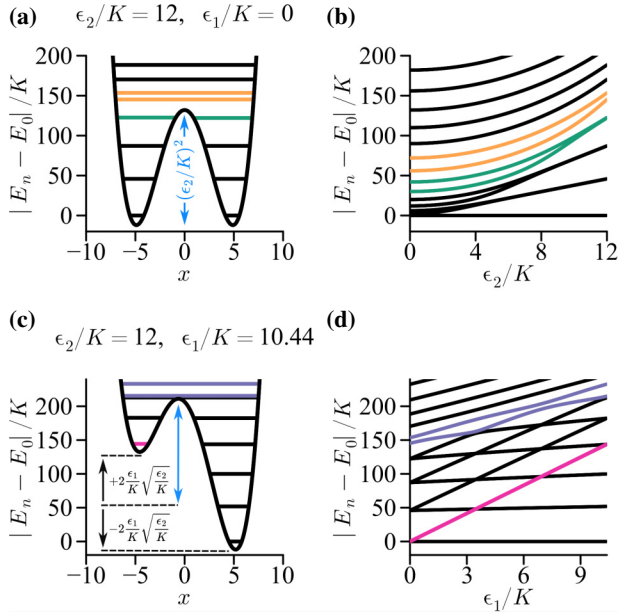

FIG. 2. Symmetric and asymmetric double-well spectrum. (a) Effective double-well potential energy $V(x)$, represented here with the quantum energy levels. (b) Transition spectrum $|E_n - E_0|/K$ of the parametric oscillator Hamiltonian as a function of ϵ_2 controlling the barrier height [27]. The levels highlighted in green become degenerate at $\epsilon_2/K \approx 12$, while the next pair of levels (highlighted in orange) is not yet degenerate at this value of ϵ_2/K. (c) Same as (a) but with asymmetry. (d) The transition spectrum as a function of ϵ_1 controlling the asymmetry. The ground level in the shallow well is highlighted in pink. The pair of levels at the barrier top is highlighted in violet. Note the oscillation of the energy separation between these two levels as a function of ϵ_1/K.

to the data in Fig. 3. From the flux dependence of both ω_a and K, we can fit a model for the SNAIL [20] to extract $g_3/3 = 2\pi \times (-5.6)$ MHz and $g_4/4 = 2\pi \times (-74)$ kHz. The values of Ω_1 and Ω_2 are directly proportional to the microwave amplitude we apply to our sample and, therefore, we have precise control over ϵ_1 and ϵ_2. Details on this calibrations are provided in Appendixes.

To measure the activation rate of our system, the states localized at the bottom of the wells need to be prepared and monitored as a function of time. By turning on the squeezing drive, and waiting five times the single-photon lifetime, we prepare the oscillator in its steady state. We observe the bifurcation of our SNAIL oscillator by homodyning the emitted radiation activated by a tone parametrically coupling the parametric oscillator with the on-chip readout resonator, itself coupled to our quantum-limited amplifier detection line [17]. The homodyne signal clearly shows the typical pair of stable oscillations out-of-phase by 180°. Importantly, the photons emitted by the oscillator during readout are continuously replenished by the squeezing drive: the driven oscillator in the presence of dissipation

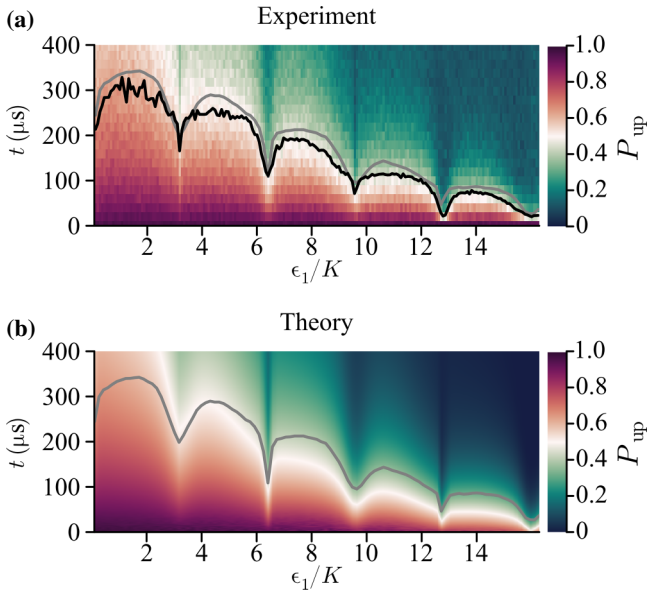

FIG. 3. Population of the shallow well as a function of time and of the asymmetry, theory vs. experiment. Data is shown for $\epsilon_2/K = 10.2$. (a) and (b) Probability of being in the shallow well as a function of time and ϵ_1/K. The curve in black represents the decay time τ of the exponential population decay. The gray curve is the theoretical lifetime fitted from the simulation to 220 mK in (b), overlaid for comparison. Resonances with characteristic widths are apparent. Notice that these widths alternate between narrow and broad. Also note that the maximum of the first lobe occurs at finite asymmetry and therefore the lifetime is larger at finite asymmetry than at zero asymmetry, which is unexpected. Data is collected and fitted from zero to 900 μs but the portion from 400 to 900 μs is not shown. The theory plot in (b) is obtained from a Lindblad model with single-photon gain and loss (see the main text for details). This simulation reproduces the key features observed in the experiment, including the locations of the resonances, the alternating pattern of narrow and broad widths, and the maximal lifetime occurring at small finite asymmetry.

remains in one of its two quasi-steady states [32]. Acquiring a single data point for the which-well information takes 4 μs, which is typically much shorter than the activation time across the double-well parametric oscillator barrier, which is of order 100 μs. We postselect the instances when the system is initially found in the shallower well. By performing a second measurement after a variable waiting time (see Appendixes), one can detect well-switching. By repeating these measurements, one can determine the probability per unit time of witnessing an activation event and therefore obtain the activation rate for a given set of Hamiltonian parameters ϵ_1/K and ϵ_2/K, which we fit using the Lindbladian model from this data.

In Fig. 3(a), we show measurements of the population dynamics of the wells for different values of the asymmetry, controlled by ϵ_1/K. For these measurements the squeezing amplitude is set to $\epsilon_2/K = 10.2$. The probability, as a function of time, of being in the initial well is well approximated by an exponential decay (see Appendixes). This timescale τ of this exponential is a direct measurement of the activation rate $(1/\tau)$ and we plot it as a black line on top of the data. In Fig. 3(b), we show a theory plot from a Lindbladian model fitted to the data [see Eq. (C1) in Appendixes]. It includes single-photon loss at rate $\kappa/K = 0.011$ and gain associated with a temperature of 220 mK. The theory fit has an associated activation time plotted as a gray line in both Figs. 3(a) and 3(b).

We observe unexpected resonances for certain values of ϵ_1/K, where the activation rate is markedly increased. These are resonances between levels localized in different wells. The resonances for levels deep within the wells behave effectively as level crossings since the coupling is exponentially small due to the suppression of tunneling under the barrier. Therefore, these activation events occur through a two-step process: population is first transferred from the bottom of the well to eigenstates at the barrier top (i.e., those whose energies lie near the local maximum of the double-well potential) by thermal and quantum heating [14,15] and then tunnels to the other well [18]. An extensive theoretical analysis of the different heating mechanisms and the importance of the barrier-top eigenstates in KPOs is provided in Ref. [33]. Briefly summarized, thermal heating drives population into barrier-top superposition states by absorbing real photons, while quantum heating arises because photon loss in the Fock basis can appear as heating when viewed in the eigenbasis of the effective Hamiltonian. In our parameter regime, thermal heating dominates [33]. That the crossing is of over-the-barrier type is also seen from Figs. 3 and 4 by noting that the alternating width of the different resonance in Fig. 2(d) corresponds to the strength of the anticrossings of the spectrum at the barrier top [purple levels in Fig. 2(c)]. This interpretation of the data allows us to predict the location in parameter space where resonant tunneling takes place. This happens when the uncoupled levels in the right and left well align. By realizing that the energy spacing of the levels in the wells can be estimated by $S \approx 4\epsilon_2$ [27] and that the asymmetry, defined as the energy difference between the lower-lying state of each well, can be estimated from Eq. (3) as $A \approx 4\epsilon_1\sqrt{\epsilon_2/K}$ (see also [22]) we write the resonance condition as $(A = nS)$

$$\frac{\epsilon_2}{K} \approx \left(\frac{\epsilon_1}{nK}\right)^2, \tag{4}$$

where n numbers the different resonances. Whenever the levels inside the wells align, the levels close to the barrier top also align, which facilitates the passage from one well to the other. This simple formula dictates the location of the resonances (see dashed lines in Fig. 4).

We complement this analysis with a semiclassical action quantization taken here as a proxy for the quantum levels. The number of allowed quantum orbits is given by the number of action quanta enclosed by the asymmetric "figure eight" lemniscate delineating the phase space separatrix in between the wells. The orange and blue curves in Fig. 4(c) show the pairs ϵ_1/K and ϵ_2/K where the Einstein–Brillouin–Keller (EBK) [34] action quantization condition is met. That is,

$$\frac{1}{2\pi}\oint p\,dx = \hbar\left(\tilde{n}+\frac{1}{2}\right), \tag{5}$$

where $\tilde{n} = n, m$ are the quantum numbers of the shallow and deep wells, respectively. The triple intersection points of the parabolas from Eq. (4) with the equi-action curves meeting the EBK quantization condition mark the point in parameter space where a new level enters the wells in the tunneling resonances condition. We mark the triple intersections in Fig. 4(c) by (n, m), the quantum numbers of each well. At these points, where each well contains exactly n and m semiclassical orbits, we expect the resonance to broaden due to a new orbit contributing to the activation rate. This is seen as sharpening structures in Figs. 4(a) and 4(b) (see also Fig. 3 for the broadened resonances).

In Fig. 4(a), we show the measured activation time for a scan of both ϵ_1/K and ϵ_2/K. The resonances are shown to have widths that change along the scan. They are found to reflect the width of the tunneling anticrossings at the top of the barrier. This can be seen by following the purple energy curves and their tunnel splitting in Fig. 2(d). The semiclassical Hamiltonian theory predicts, quantitatively, the resonance condition and, qualitatively, their widths (see Appendixes for a full quantum treatment). To obtain absolute activation times, we employ a Lindblad model rather than the semiclassical EBK theory.

In Fig. 4(b), we show the Lindbladian model fit to the experiment. The fit requires a temperature dependence with ϵ_2 which is well approximated by a quadratic function increasing from ∼170 mK at $\epsilon_2 \approx 3$ to ∼310 mK at $\epsilon_2/K \approx 14$ (see Appendixes for the temperature extraction). This is consistent with Johnson-Nyquist thermal noise produced by the heating of the attenuators with increasing squeezing amplitude. However, as we expand in Appendixes, we note that this is merely phenomenological and more involved physics are possibly involved. Other sources for the effective temperature can be unwanted mixing Josephson terms [35] or other modes in the system [36]. A way to mitigate this temperature exists, however, and is being developed and has already been implemented elsewhere by us [37] and our colleagues [38].

We learned from this data that an asymmetric system can have a longer activation lifetime than the symmetric system, even if one of the wells is markedly shallower (see Fig. 3 at $\epsilon_1/K \approx 1$). The green-black dashed line in Fig. 4(a) shows the experimentally determined maxima of activation time τ as a function of the control parameters. The

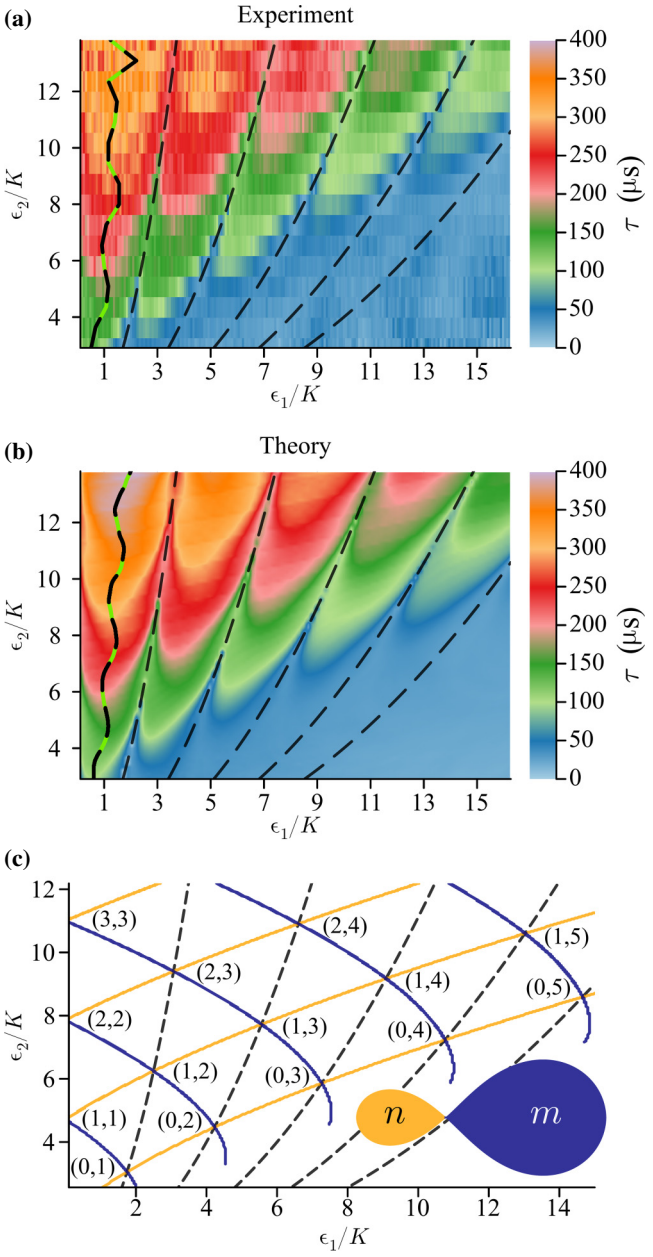

FIG. 4. Analysis of the dissipative tunneling resonances according to different models and the experiment. (a) Measurement of dissipative tunneling time τ as a function of ϵ_2/K (controlling the barrier height) and ϵ_1/K (controlling the asymmetry) in a linear color scale. (b) Theory fit from a Lindbladian model including single-photon loss and a temperature that depends on ϵ_2, growing quadratically from 170 to 310 mK (see Appendixes). The wavy green-black lines show that the maxima of τ "avoid" the resonances marked by the triple intersections. (c) Hamiltonian fit for the resonance conditions (parabolic dashed lines) and EBK's orbit quantization condition for n and m allowed quantum numbers in the small (orange) and large (blue) figure-8 lobes. The triple intersections are labeled by (n, m) quantum numbers.

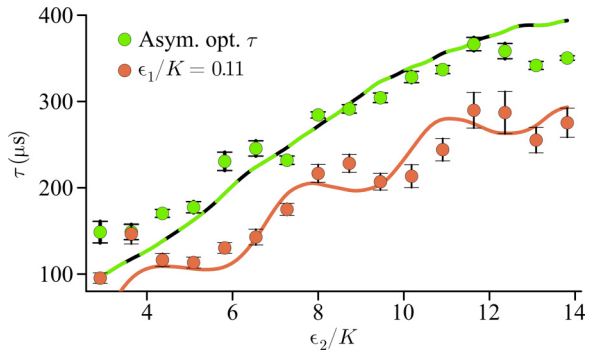

FIG. 5. Experimental (points) and theoretical (solid lines) activation time τ for (nearly) symmetric KPO and at optimal asymmetry. Depicted as a function of barrier height ϵ_2/K. We observe that a finite asymmetry can increase the activation time. Here the asymmetric case (green) is consistently above the data for the symmetric case (orange). The asymmetric optimum corresponds to the green-black lines in Figs. 4(a) and 4(b).

theoretical maxima are shown in Fig. 4(b) by the line with the same colors and agree with those we find by keeping the temperature constant in the model (not shown). The location of the maxima is nontrivial, and it is relevant to control reaction rates, or analogously because it can readily be used to extend the lifetime of a Kerr-cat qubit [17].

In Fig. 5, we show the increase of τ with the asymmetry parameter. To provide physical insight into this effect, we note that Lindblad theory predicts that τ is modulated in a steplike fashion as the quantized orbits fall under the barrier [18] (see also Appendixes). The linear drive can be exploited to break the parity symmetry of these orbits as shown in Fig. 2 and therefore avoid the steplike modulation seen in the Lindblad theory for $\epsilon_1 \approx 0$. This observation explains the trajectory of the green-black optimal curve in Figs. 4(a) and 4(b), which avoids the new resonance conditions marked by the triple intersections. In other words, quantum tunneling produces a hybridization of the classically decoupled orbits right under the barrier. The asymmetry parameter can be adjusted to minimize that hybridization, reducing the tunneling rate via the excited states.

IV. QUANTUM SIMULATION OF CHEMISTRY

The experimental observations presented here raise the question of whether they are present in other double-well systems, like the type of double-well involved in modeling chemical reactions. In chemistry, while harmonic modes coupled to spins are often used to model charge transfer in a simplified framework [6], a true double-well description offers a more natural representation in the adiabatic regime, where the potential energy landscape plays a crucial role. The true double-well potential provides a general framework that accurately captures essential features of numerous chemical processes, such as proton transfer, isomerization, and proton-coupled electron transfer [16].

We run a Lindbladian simulation for the chemical system to investigate if our experimental observations also manifest here. For this, we use the chemically inspired Hamiltonian $\hat{H}/\hbar = \hat{p}^2/2 + k_4\hat{x}^4 - k_2\hat{x}^2 + k_1\hat{x}$, including single-photon loss and gain with rate $\kappa/k_4 = 0.025$ and at a constant temperature of $n_{\text{th}} = 0.05$. These parameters lie in the ranges accessible by our system. The Lindblad approach is valuable because it produces chemical dynamics with well-defined reaction rates and qualitatively agrees with experimental observations in the weak coupling regime [6,39–41]. In electron-transfer chemistry, a typical choice of dissipation is Ohmic noise, which under standard approximations translates into single-photon loss and gain represented by the dissipators of the Lindblad model [42].

With this framework, we answer our question affirmatively: our experimental observations are predicted to be present in other double-well systems. On the one hand, the green-black line in Fig. 6(a) depicts the maximum lifetime as a function of well asymmetry and well depth, showing that—just like in our experiment [Figs. 4(a) and 4(b)]—a small asymmetry increases the lifetime significantly [see also Figs. 5 and 6(b)]. On the other hand, Fig. 6(c) depicts a horizontal linecut of Fig. 6(a) and clearly reveals the same width alternation (broad-narrow-broad) as discovered and explained in our experiment (see Fig. 3). The finding of these two unexpected effects shows that our asymmetric Kerr parametric oscillator setup is already able to produce meaningful predictions for chemical quantum rate theory.

Double-well systems have been extensively studied in various contexts [42,43], including in superconducting circuits [44–47]. However, we speculate that the unique combination of precise real-time microwave control, complete tunability over Hamiltonian parameters, experimental stability, fast repetition rates, and high-fidelity readout in our setup explains why we observed the effects not previously reported.

Based on these results, we proposed a hardware modification to our setup that implements a one-to-one single-transmon quantum simulation of tautomerization reactions in Malonaldehyde (cis-cis) and proton transfer reactions between the DNA base pairs guanine-cytosine [16]. The key to this simulator is that, for *realistic circuit parameters*, the Hamiltonian cross-terms $\propto x^2p^2$ and the relativistic-like $\propto p^4$ term become irrelevant perturbations [these arise from the Kerr term $\hat{a}^{\dagger 2}\hat{a}^2$, which in turn arises from the x^4 term as perturbations, see Eq. (1)]. Also, our system allows for a clean microwave control of effective temperature. Injecting noise through a microwave drive port is an established method in circuit QED to increase the effective temperature (n_{th} in the Lindblad

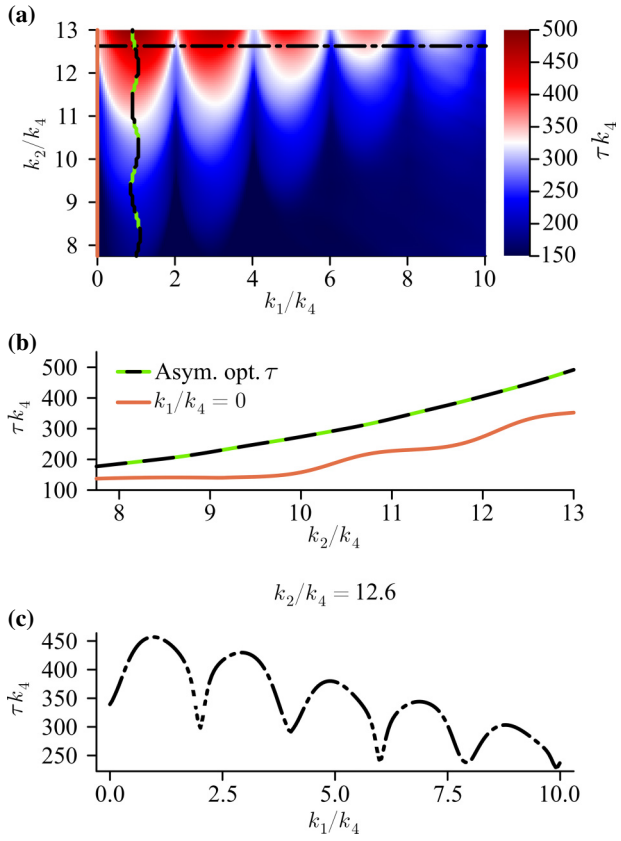

FIG. 6. Lindbladian simulation of an ordinary double-well system. (a) Dynamics simulated as a function of well asymmetry k_1/k_4 and well depth k_2/k_4. The color code marks the activation time [compared to Fig. 4(b)]. The green-black line shows the maximum activation time and the orange line marks the symmetric case ($k_1 = 0$). (b) Comparison of the activation time for the ordinary symmetric ($k_1 = 0$) double-well and the (optimal) activation time along the green-black line in (a) as a function of well depth k_2/k_4. (c) Activation time as a function of asymmetry for $k_2/k_4 = 12.6$ [black dashed line in (a)], showing resonant tunneling (as in Fig. 3, see also [6]). Note that, as in the parametric oscillator Fig. 3, the linewidths alternate from broad to narrow.

model) of a system [48]. We emphasize that our microwave tones are generated using arbitrary waveform generators and can therefore create nearly arbitrary noise spectra. Controllable single-photon dissipation has been demonstrated for KPOs [18,37]. By selecting the frequency of the dissipated photons, this mechanism can be used to engineer cooling (reduction of n_{th}) [37] or to increase the single-photon loss rate (κ in the Lindblad model) [18]. Beyond this, exotic forms of dissipation have been proposed [31,35]. Finally, controllable interactions between two KPOs have been generated in our setup, which can create non-Markovian dynamics [49]. All these allow for the experimental exploration of chemical dynamics across a wide range of parameter spaces [6,50] in this type of single-transmon parametric quantum simulator.

We conclude this section by giving a perspective on how this approach can be generalized beyond a single SNAIL transmon. Controllable interactions of form $\hat{a}_1^\dagger \hat{a}_2 + \mathrm{h.c.}$ have been implemented for KPOs in superconducting circuits [51]. This interaction translates to a bilinear coupling $\hat{x}_1\hat{x}_2$, opening promising avenues for applications in chemistry. The description of concrete chemical systems that can be mapped to multiple coupled KPOs is the subject of ongoing work and will be presented in a forthcoming paper. Furthermore, the superconducting platform itself supports strong scalability, with current systems already exceeding 1000 transmons [52].

V. CONCLUSION

We reported the measurement of the activation rate in a continuously tunable asymmetric Kerr parametric oscillator with dissipation and observed a fine structure that, to the best of our knowledge, was unknown in the literature. Our experiment shows that the activation rate displays resonances whenever a level close to the barrier top aligns with one in the other well. We derive an analytical formula that predicts the occurrence of these resonances as a function of asymmetry and well depth. Furthermore, we discover that these tunneling resonances alternate in width between narrow and broad lines as the asymmetry and well depth are changed. We trace this effect back to the alternating strengths of level anticrossings in the spectrum close to the barrier top. This shows that the activation is of over-the-barrier type (i.e., not via direct quantum tunneling by the low-lying states), as predicted [14,22,53]. We are thus able to learn the level structure near the barrier top without having to prepare these excited states.

Our control over the well asymmetry indicates that quantum parametric oscillators can implement analog quantum simulation of chemical reaction dynamics [16]. This allows, for instance, the analog simulation of proton tunneling, and, e.g., the study of transfer reactions between the guanine-cytosine DNA base pairs, appears within reach of current Kerr parametric oscillator technology [16].

We also note the importance of this system for quantum computation since qubits can be encoded in the well-state manifold [17,27]. In this regard, two contributions of the present work deserve to be highlighted. The first one is the increase in the activation timescale τ by a fine control of the asymmetry. This leads to a reduction in bit-flip errors [54] with no extra hardware requirements. The second contribution is the demonstration of the operation of a highly asymmetric parametric oscillator in the quantum regime. We provide direct evidence that the static effective description is not compromised under strong linear drives, which are required for fast gates [27] and implementations of hardware-efficient readout schemes [55].

After writing this paper, we were made aware of a similar experiment at Rice University using trapped ions

to create an asymmetric double-well to simulate electron transfer [42].

ACKNOWLEDGMENTS

We acknowledge useful discussions with Q. Su, A. Ding, B. Brock, and M. Dykman. Remarks by V. Joshi and A. Koottandavida have improved the manuscript. This research was sponsored by the Army Research Office (ARO) under Award No. W911NF-23-1-0051. The views and conclusions contained in this document are those of the authors and should not be interpreted as representing the official policies, either expressed or implied, of the Army Research Office (ARO), or the U.S. Government. The U.S. Government is authorized to reproduce and distribute reprints for Government purposes notwithstanding any copyright notation herein. V.S.B., E.G., and M.H.D. acknowledge partial support from the National Science Foundation Center for Quantum Dynamics on Modular Quantum Devices (CQD-MQD) under Award No. 2124511.

A.C.C.dA, R.G.C., and M.S. analyzed the data and modeled the experiment. A.C.C.dA, R.G.C., M.S., and M.H.D. wrote the manuscript. P.E.V. supported the data analysis. All authors contributed to the manuscript. R.G.C. and M.S. conceptualized the experiment and collected data. N.E.F. fabricated the device. B.A., D.G.A.C., P.K., E.G., and V.S.B. validated the relevance and utility to chemistry and provided theory support. M.S. coordinated the interdisciplinary collaboration and led the revision process. M.H.D. and R.G.C. supervised the research.

DATA AVAILABILITY

The data are not publicly available. The data are available from the authors upon reasonable request.

APPENDIX A: EXPERIMENTAL SETUP

The wiring diagram is shown in Fig. 7. The lines from left to right are as follows: (1) the microwave pump for the SNAIL-Parametric-Amplifier (SPA) [56], (2) the readout output line, (3) the input line for the dispersive readout, (4) the two-photon drive at frequency $\omega_2 \approx 2\omega_o$, (5) the one-photon drive at frequency $\omega_1 = \omega_2/2$, (6) the input line for the parametric readout, which is the readout method utilized in this paper. Additionally, there are two twisted-pair cables that provide a DC signal to magnet spools that create a magnetic flux for the SPA and the SNAIL-transmon sample. Our setup is similar to the one first described in [17].

APPENDIX B: CALIBRATIONS OF EXPERIMENTAL PARAMETERS

1. Measurement of Kerr coefficient and frequency

The Kerr coefficient K is extracted by spectroscopy. A saturating probe drive ω_{pr} is applied to the SNAIL transmon operated with $\epsilon_2 = 0$. Varying the probe drive frequency and measuring the response via dispersive readout, results in the data are shown in Fig. 8. The spectrum shows two clear dips, which correspond, from lower frequency to higher frequency, to the two-photon $gf/2$ transition and the ge transition (the SNAIL levels are labeled following the atomic physics convention in increasing energy order g, e, f). Note that the measured ω_{ge} is a good approximation for ω_a used in [Eq. (2)]. We then extract the Kerr frequency by using the relation $\omega_{ge} - \omega_{gf/2} = K$. Fitting two Gaussian peaks to the spectrum in Fig. 8, we find $K/2\pi = (528 \pm 10)$ kHz. This measured value differs from the fitted one (465 kHz) by 12% and it is not used in the simulations. These measurements, when taken as a function of the biasing flux Φ of the superconducting loops, allow for a calibration of the SNAIL nonlinear parameters g_3, g_4. In Fig. 9, we show a flux scan of our sample with measured frequencies, Kerr nonlinearities, and the fit by the model presented in [20].

2. Calibration of relative phase between squeezing drive and linear drive

Quantum coherent Rabi-like oscillations as a function of this phase ϕ are shown in Fig. 10(a) [17]. For $\phi = 0$, this drive is position-like and lifts the degeneracy between the two wells [see Figs. 2(c) and 11(a)]. This energy difference induces the Rabi-like oscillation. For $\phi = 90^\circ$ [Fig. 10(a)], the linear drive is momentum-like (the Hamiltonian term is $\propto \hat{p}$), thus not breaking the symmetry between the wells [see Fig. 11(d)]. The well asymmetry is determined by $\epsilon_1 \cos\phi$ and is therefore first-order insensitive to phase drifts of a few degrees around $\phi = 0$, which is the precision of our calibration.

3. Calibration of the parametric squeezing drive amplitude ϵ_2 and linear drive amplitude ϵ_1

In the experimental setup, the drive amplitudes are directly controlled by a digital to analog voltage converter. To calibrate the strength of the drive in MHz we measure time-resolved Rabi oscillations as a function of the digital control of the squeezing drive ϵ_2. The experimental data is shown in Fig. 12(a). The oscillations of the observable $\hat{X} = (|\alpha\rangle\langle\alpha| - |-\alpha\rangle\langle-\alpha|)$ occur at a rate $\Omega_{\text{cat}}(\epsilon_2) \approx \Re(4\epsilon_1\alpha^*)$ where $\alpha = \sqrt{\epsilon_2/K}$ and the approximation is valid for $|\alpha| > 1$. Using, also, that for $\epsilon_2 = 0$ the oscillation has a frequency of $2\epsilon_1$ [17], just like for an ordinary transmon, we obtain ϵ_1 in MHz completing the calibration of the drive amplitudes. To be clear, we can

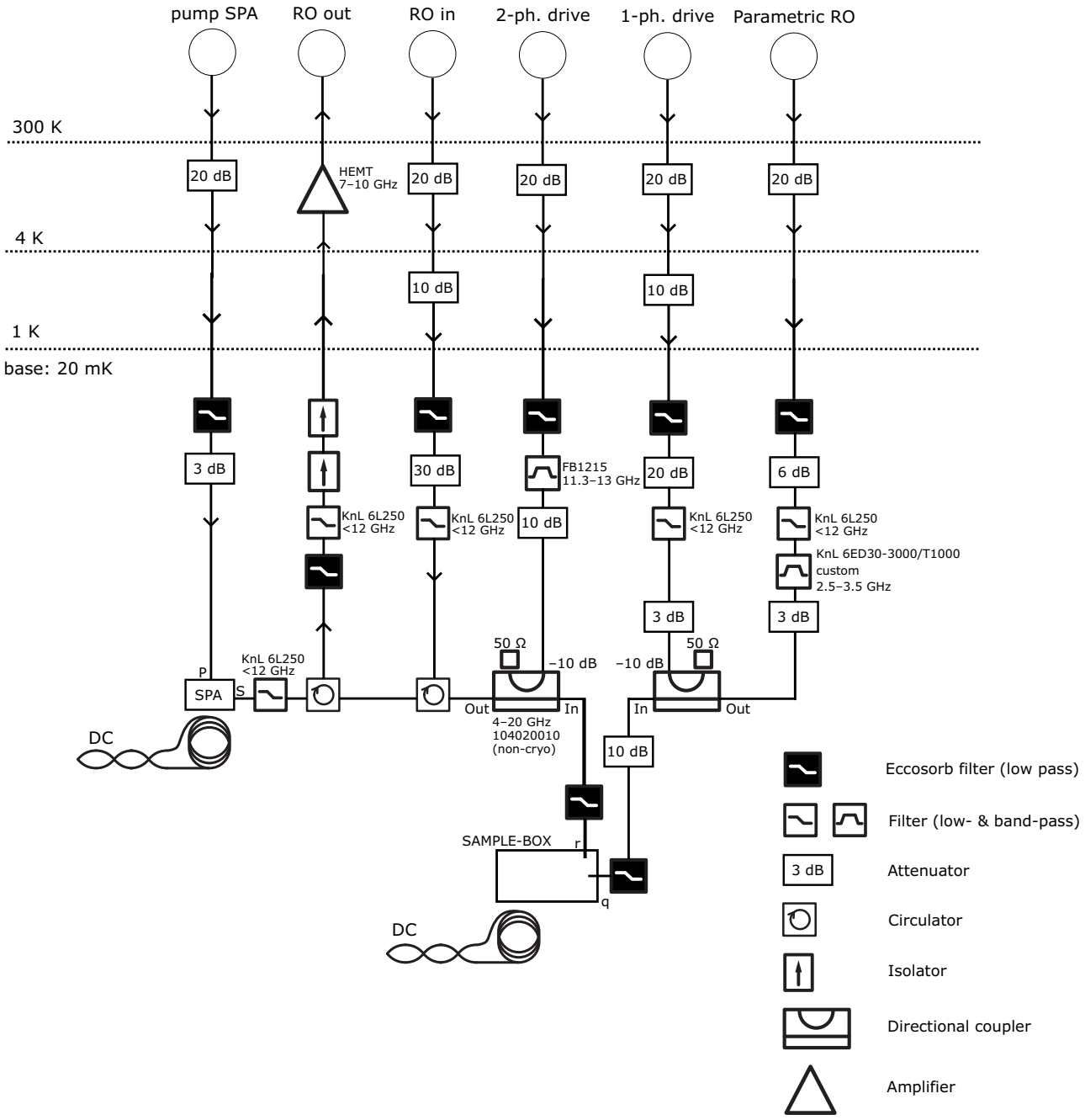

FIG. 7. Wiring diagram. A legend for the main elements is provided at the bottom right. The approximate temperatures for different stages are shown on the left. The sample is contained in the sample box.

rewrite this relation as $\langle \hat{a}^\dagger \hat{a} \rangle = \epsilon_2/K = \Omega_{\text{Rabi}}(\epsilon_2)^2/16\epsilon_1^2$, where $\langle \hat{a}^\dagger \hat{a} \rangle$ is the average photon number of the coherent states. By extracting the Rabi rate Ω_{cat} for each voltage of the digital control of ϵ_2 and using the previously determined value of ϵ_1, we find $\langle \hat{a}^\dagger \hat{a} \rangle$ as a function of the digital control of ϵ_2. The data is shown in Fig. 12(b) and shows a linear relationship between the applied voltage for the drive and the average photon number. The slope of the linear fit (together with the previously extracted value of Kerr) determines the proportionality constant between the digital to analog converter in volts and the drive amplitude ϵ_2 in MHz as required by the Hamiltonian description.

APPENDIX C: COMPLEMENTARY ANALYSIS

1. Parameter extraction

Theory parameters K, Δ, κ, and n_{th} are obtained by fitting the Lindbladian model,

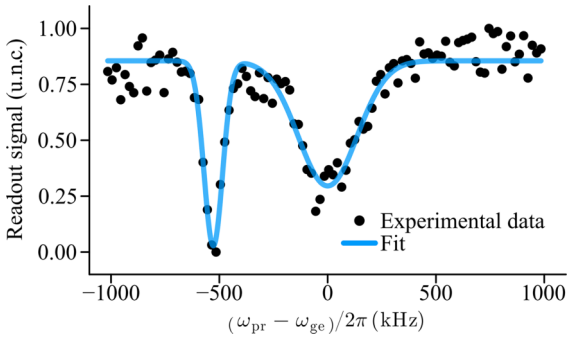

FIG. 8. Continuous-wave spectroscopy measurement showing the readout response as a function of the probe tone frequency. From left to right, the pronounced dips in the signal show the $gf/2$ and ge transitions of the SNAIL transmon. Those occur at $(\omega_{ge} - K)/2\pi$ and $\omega_{ge}/2\pi$, respectively. Fitting to this experimental data, we extract a Kerr value of $K/2\pi = (528 \pm 10)$ kHz. However, this value is not used in any of the simulations (theory fitted 465 kHz is used instead).

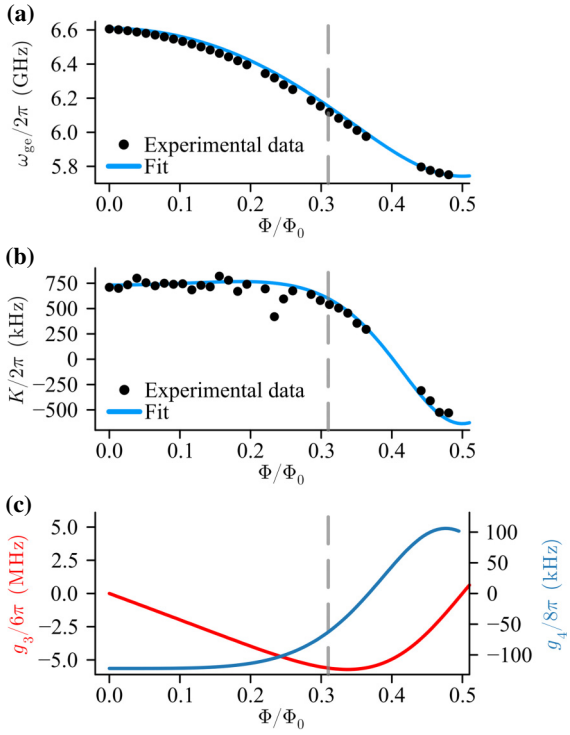

FIG. 9. Extraction of nonlinearities from fit to frequency and Kerr parameter. (a) Spectroscopic measurement of the oscillator's frequency and (b) its Kerr nonlinearity as a function of flux as extracted from the ge and $gf/2$ transitions (see Fig. 8). Solid lines are a simultaneous fit of frequency and nonlinearity from the SNAIL circuit model [20]. We remark that several arrangements of parameters fit the data satisfactorily, producing a large correlation and errors. In (c) we show the third- and fourth-order nonlinearities as extracted from the fit. The vertical dashed line represents the flux operating point for the experiments in this paper.

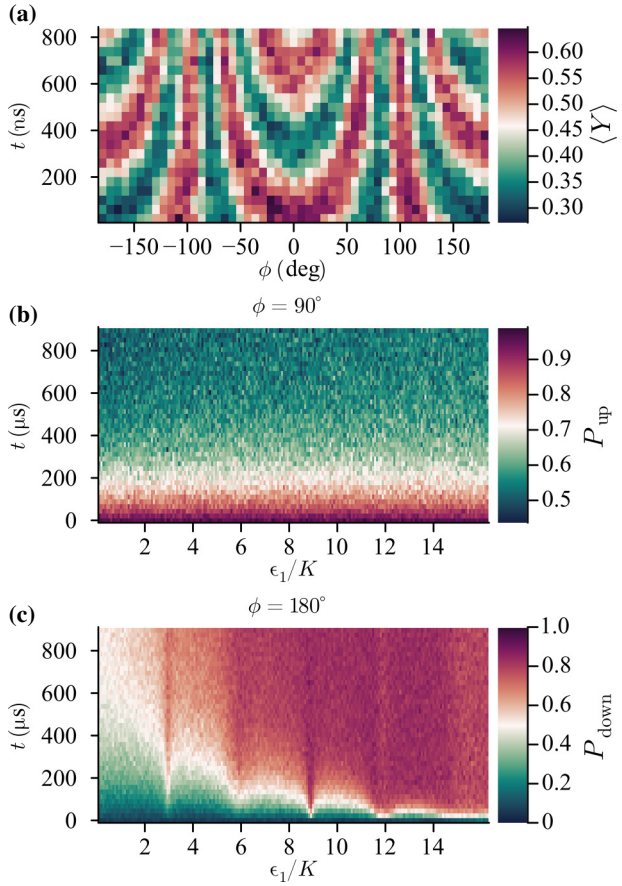

FIG. 10. Effects of the relative phase of the linear drive. (a) Time-resolved quantum coherent oscillation in $\hat{Y} = i|\alpha\rangle\langle -\alpha| - i|-\alpha\rangle\langle\alpha|$ as a function of relative phase ϕ between the squeezing and linear drives [17]. This measurement shows Rabi-like oscillation between the cat states created by superposing states in different wells. The oscillation frequency is a direct measure of the asymmetry. (b) Data taken for $\epsilon_2/K = 8.7$. Linear drive with a relative phase of $\phi = 90°$. The wells are slightly deformed but they remain mirror symmetric to each other and no resonances are visible. (c) Data taken for $\epsilon_2/K = 8.7$. As in Fig. 3(a), we measure the activation rate for different asymmetries, but now caused by a linear drive with a phase $\phi = 180°$ instead of $\phi = 0°$. The flipped phase results in an exchange of the left and right well, meaning that now the left well is the deeper one. In the experiment, we still initialize in the shallower (now right) well, but now measure the time-resolved population of the deeper (now left) well. As a result, the population of the left well is initially zero and then increases over time. We again observe trends and features, such as the resonant tunneling also seen in Fig. 3(a). This confirms that the 180° phase shift only exchanges the roles of the wells, but otherwise exhibits the same physical phenomena.

$$\dot{\hat{\rho}} = -\frac{i}{\hbar}[\hat{H}_{\text{eff}}, \hat{\rho}] + \kappa(1 + n_{\text{th}})\mathcal{D}[\hat{a}](\hat{\rho}) + \kappa n_{\text{th}}\mathcal{D}[\hat{a}^\dagger](\hat{\rho}) \tag{C1}$$

to the experimental data in Fig. 4(a), starting from the independently measured values. Here $\hat{H}_{\text{eff}}$ is the Hamiltonian from Eq. (2) (with $\phi = 0$). First, Kerr is found by fitting

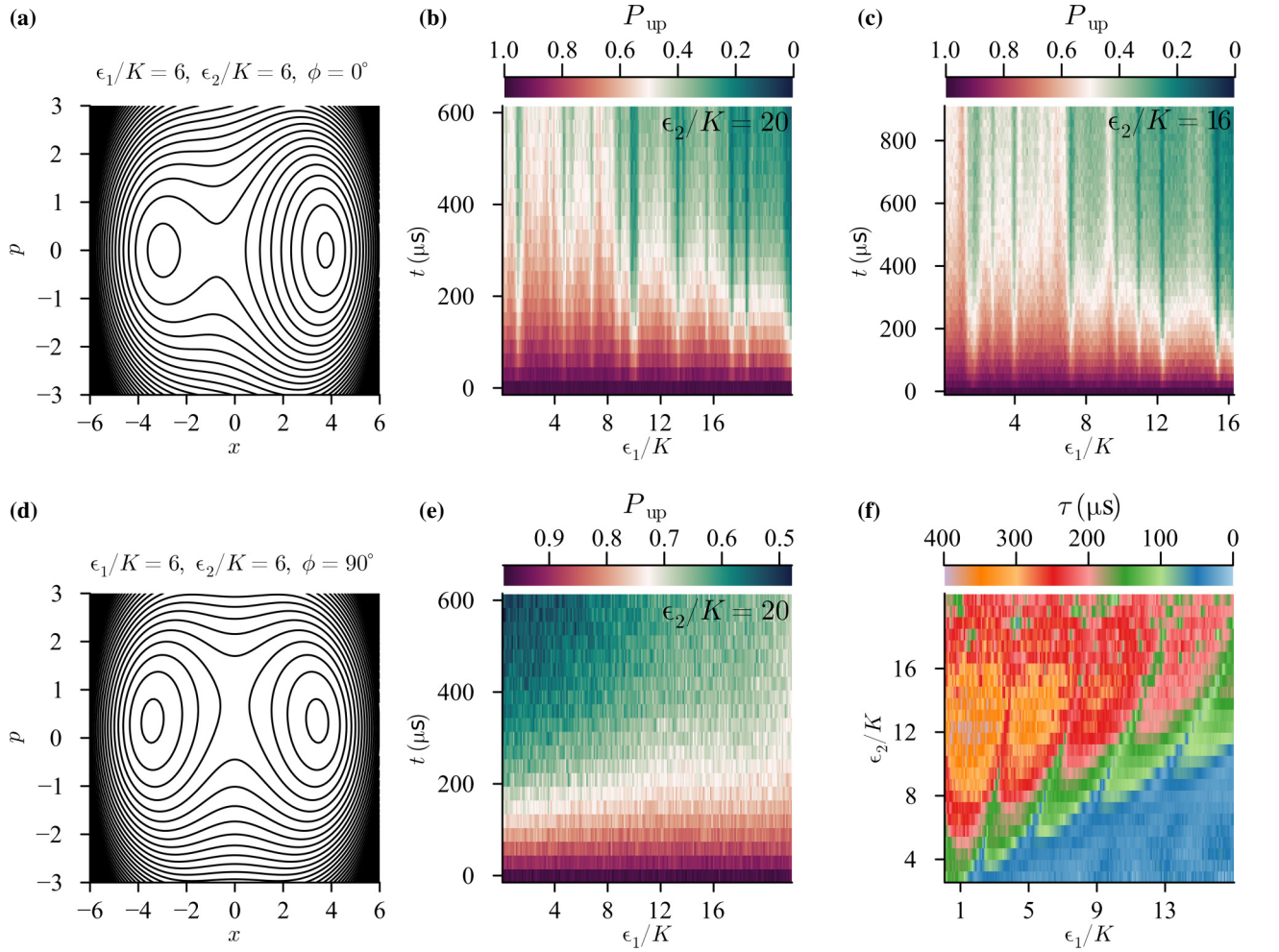

FIG. 11. Emergence of resonance-like features depending on different parameters. (a)–(c) Relative phase $\phi = 0°$ between linear drive and squeezing drive. (a) Equienergy contours of the classical rotating wave approximation parametric oscillator Hamiltonian with linear drive. The linear drive raises the left well and breaks the symmetry between the two wells within the rotating wave approximation. (b) Same experiment as in Fig. 3(a), now at $\epsilon_2/K = 20$. A "forest" of resonances is now visible besides the rotating wave approximation resonances from condition Eq. (4). (c) Changing the photon number to $\epsilon_2/K = 16$ changes the resonance pattern. Note the different widths. (d) and (e) Relative phase between linear and squeezing drive of $\phi = 90°$. (d) Equienergy surfaces in the presence of the linear drive within the rotating wave approximation, showing that the symmetry between wells is preserved and a small deformation in the p direction is visible. (e) Same measurement as in (b) but with 90° shifted phase ϕ. This change in phase is sufficient to remove all of the resonances, while the amplitude of both drives remains high. (f) Extension of data in Fig. 4(b). Now the squeezing amplitude extends beyond $\epsilon_2/K = 14$ up to $\epsilon_2/K = 19$. The data in (b) and (c) shows up as flecks of short lifetime (blue) that are not captured by the rotating wave approximation.

the location of the resonance parabolas in the ϵ_1–ϵ_2 plane of Fig. 4(a) to those in Fig. 4(b) since these features are very robust to changes in Δ, κ and n_{th}. This resulted in a Kerr of $K/2\pi = 465$ kHz. Next, for each value of ϵ_2, n_{th} is fitted so that the resulting timescale τ best quantitatively agrees with its experimental counterpart. With this, we report a quadratic dependence of the effective temperature T on ϵ_2, see markers in Fig. 13. We use a quadratic fit of n_{th} on the theory, extending continuously those values of ϵ_2 for which there is no experimental record of n_{th}, see solid line in Fig. 13. Lastly, as reported in [18,28], we fine-tuned $\Delta/2\pi = -558$ kHz and $\kappa/2\pi = 5.1$ kHz (corresponding to a single-photon lifetime of 31 μs) to match the phase of the steplike oscillations of τ in the theory to those of the experiment.

2. Possible contributions to the effective temperature and mitigation techniques

The extracted effective temperature has a quadratic dependence on ϵ_2/K, as shown in Fig. 13. In turn, ϵ_2/K is directly proportional to the voltage V from the digital controller electronics (see Fig. 12). Therefore, $T \propto (\epsilon_2/K)^2 \propto V^2$, which is the form of Johnson-Nyquist noise. A natural

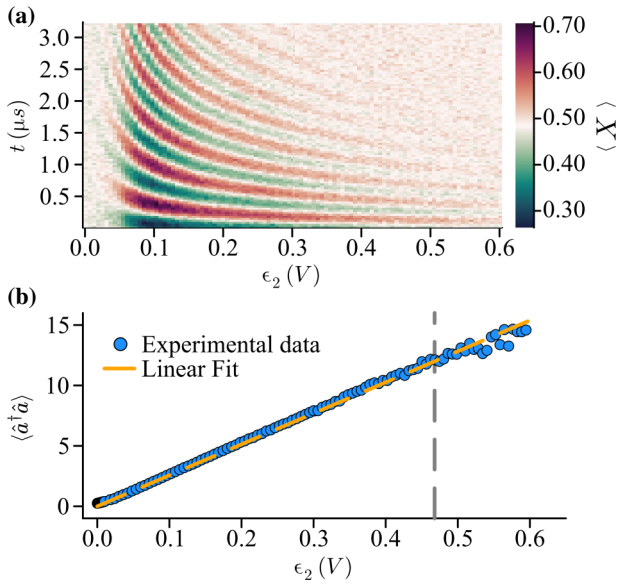

FIG. 12. Calibration of squeezing drive strengths. (a) Time-resolved quantum coherent Rabi-like oscillations as a function of squeezing amplitude. The squeezing amplitude is controlled by the voltage of the digital controller. (b) Photon number $\langle \hat{a}^\dagger \hat{a} \rangle$ as a function of applied voltage for the digital control of squeezing drive ϵ_2. The experimental data points are obtained from (a) using $\langle \hat{a}^\dagger \hat{a} \rangle = \epsilon_2/K = \Omega_{\text{Rabi}}^2/16\epsilon_1^2$, where ϵ_1 is the asymmetry for $\phi = 0$. A linear fit allows us to convert the voltage set by the digital control of ϵ_2 to the squeezing drive ϵ_2 in MHz. The primary analysis focuses on data measured with up to $\epsilon_2/K = 13.8$ (vertical dashed gray line).

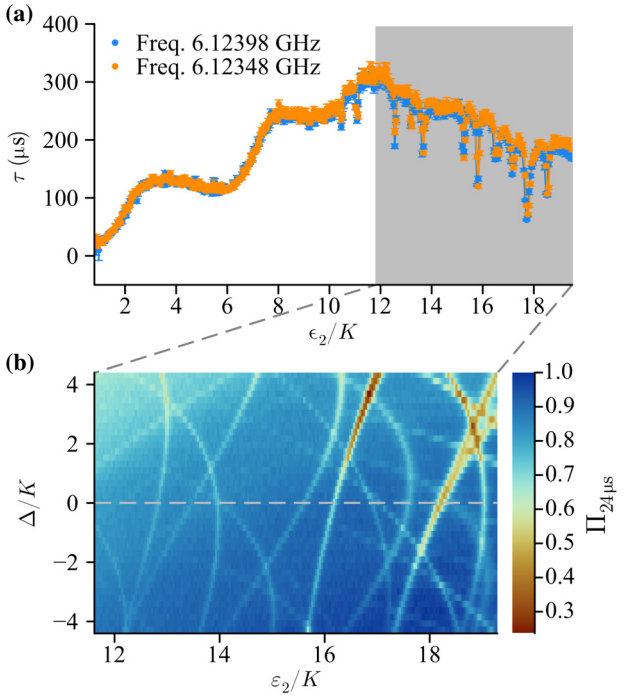

FIG. 14. Resonance-like features not explained by the rotating wave approximation model. (a) Coherent state lifetime as a function of photon number ϵ_2/K (at $\epsilon_1 = 0$). The blue and red curves are the same measurement repeated after a 24 h time difference. The frequency was recalibrated to account for a small drift. The lifetime saturates at around 300 μs. For large photon numbers ϵ_2/K, resonance-like features appear. The location of these is stable within the 24 h time difference. (b) The parametric oscillator is initialized in one of the wells and after 24 μs the remaining population in this well is measured. This is a proxy for the coherent state lifetime and thus allows us to identify resonances like in (a), which emerge as a low remaining population. This is measured as a function of photon number ϵ_2/K and detuning $\Delta = (\omega_2/2) - \omega_a$ between the first subharmonic of the squeezing drive and the SNAIL transmon resonance frequency. At $\epsilon_2/K = 15$ and $\Delta/K = -2$, a crossing between resonances is visible. Another feature occurs at $\epsilon_2/K = 19$ and $\Delta/K = 2$, where the line of a resonance splits into two.

explanation for this effective temperature dependence is thus a heating attenuator or 50 Ω termination (see Fig. 7 for the attenuator configuration). This could be mitigated by improved thermalization of attenuators, filters, and terminations. Possible other contributions are the noise temperature of the room-temperature electronics, leakage via hybridization with the buffer mode (see Fig. 14 for some experimental evidence of that in the very strong drive regime), and unwanted higher-order loss channels

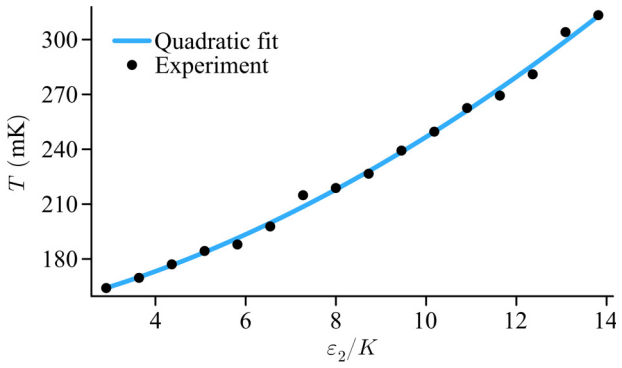

FIG. 13. Temperature dependence on ϵ_2. Round markers were extracted from experimental data in Fig. 4(a) by fitting to theory.

in the SNAIL loop. Promising engineering solutions to these issues are on-chip filters [28], careful detuning of the buffer mode [36], and the Symmetrically Threaded SQUID as a replacement for the SNAIL [57]. Regardless of the source of heating, engineered dissipation has been demonstrated for cooling of superconducting circuit KPOs [37,38] and is an effective mitigation technique if lower effective temperatures are desired.

3. Exponential decay

A crucial step in our data processing relies on fitting the activation dynamics with exponential decays. The experimental sequence is shown in Fig. 15(a) and three

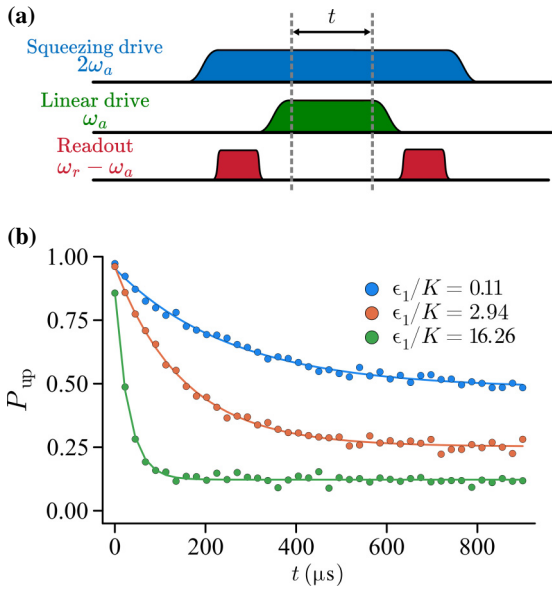

FIG. 15. Pulse sequence and typical decay curve for determination of activation time. (a) Pulse sequence for the determination of the activation time. The squeezing drive is turned on adiabatically. This is followed by a measurement of the which-well information, projecting the parametric oscillator into either of the wells. Then the linear drive is turned on adiabatically. Next, the state evolves for a variable time t, during which both the squeezing and linear drive remain on. After that, the linear drive is turned off adiabatically. Finally, the which-well information is measured again to find the remaining population. (b) Decay of a coherent state initiated on the shallower well for different asymmetry values ϵ_1/K. Experimental data are dots, and solid lines are exponential fits. For a small well asymmetry ϵ_1/K, the probability to be in the shallower well decays to 0.5. For increasingly large asymmetry, the steady-state population is no longer equally distributed between both wells, becoming increasingly biased toward the deeper well.

exemplary decay curves for different values of the asymmetry are shown in Fig. 15(b). The data with the corresponding exponential fits is shown in Fig. 3(a). We remark that each of the curves is well described by an exponential decay. Next, we notice that for small asymmetry $\epsilon_1 = 0.1$ the steady state population of the shallower well is around 50%. This is because for a symmetric double-well the probability of being in either well is identical by construction, thus leading to equal steady-state populations. On the other hand, with increasing asymmetry, the tunneling rates from one well to the other become asymmetric, leading to a bias toward the deeper well. This is represented in our data, where for increasingly large asymmetries, the steady-state population of the shallower well is reduced.

4. Control experiment for the relative phase dependence of the linear drive

The relative phase ϕ between the squeezing drive and linear drive is determined by searching for the phase of maximum Rabi rate, which occurs at $\phi = 0$. The calibration measurement is shown in Fig. 10(a). This additional degree of freedom allows for several control experiments. To confirm that the resonant features we measure are actually caused by the controlled symmetry breaking and are not for example just power-dependent nonlinear resonances [58,59] or due to Stark shifting into resonance with spurious modes [60,61], we measure the activation rate for a symmetric and an asymmetric double-well, both under an equally strong linear drive. To achieve this, we set the linear drive phase $\phi = 90^\circ$ and $\phi = 180^\circ$, respectively. The resulting measurement is shown in Figs. 10(b) and 10(c) [see also Fig. 11(e)]. We note that the resonances are not present for $\phi = 90^\circ$, thereby proving that they are indeed a controlled effect from the symmetry breaking in the parametric oscillator.

As discussed in Sec. III, we have full control over the Rabi phase [see Fig. 10(a)] which controls how the symmetric double-well is perturbed. A phase of $\phi = 0^\circ$ applies a drive that lifts the "left" well [see Fig. 11(a)] and a phase of $\phi = 90^\circ$ does not break the symmetry between the wells [see Fig. 11(d)]. If a Rabi phase of $\phi = 180^\circ$ is applied, then the definitions of left and right well swaps, meaning the right well becomes the shallower well and the left well becomes the deeper well. We can then make a control experiment where we initialize the system in the shallower (now right) well and then measure the population of the left well as a function of time and asymmetry. The resulting data [Fig. 10(c)] shows the same increase in tunneling rate with larger asymmetry ϵ_1/K and resonances at specific values. The observation of the same physical phenomena confirms our understanding of the system and validates our explanations of the observed effects.

5. Lifetime along resonances

In Fig. 16 we display the lifetime along the first four dashed parabolas of Fig. 4(b). As per resonance condition Eq. (4), an increase in ϵ_1/K corresponds to an increase in ϵ_2/K when following the parabolas. Therefore, we expect the lifetime to increase along the parabolas, which we observe in Fig. 16. The steplike behavior is a consequence of activation assisted tunneling close to the separatrix between the wells (see Ref. [18]).

6. Semiclassical analysis

In Fig. 17, we provide a succinct pictorial view of the semiclassical mechanisms behind the features in Fig. 4.

APPENDIX D: FULL QUANTUM HAMILTONIAN TREATMENT

In this appendix, we show that the physics captured by the semiclassical analysis used to explain the data is

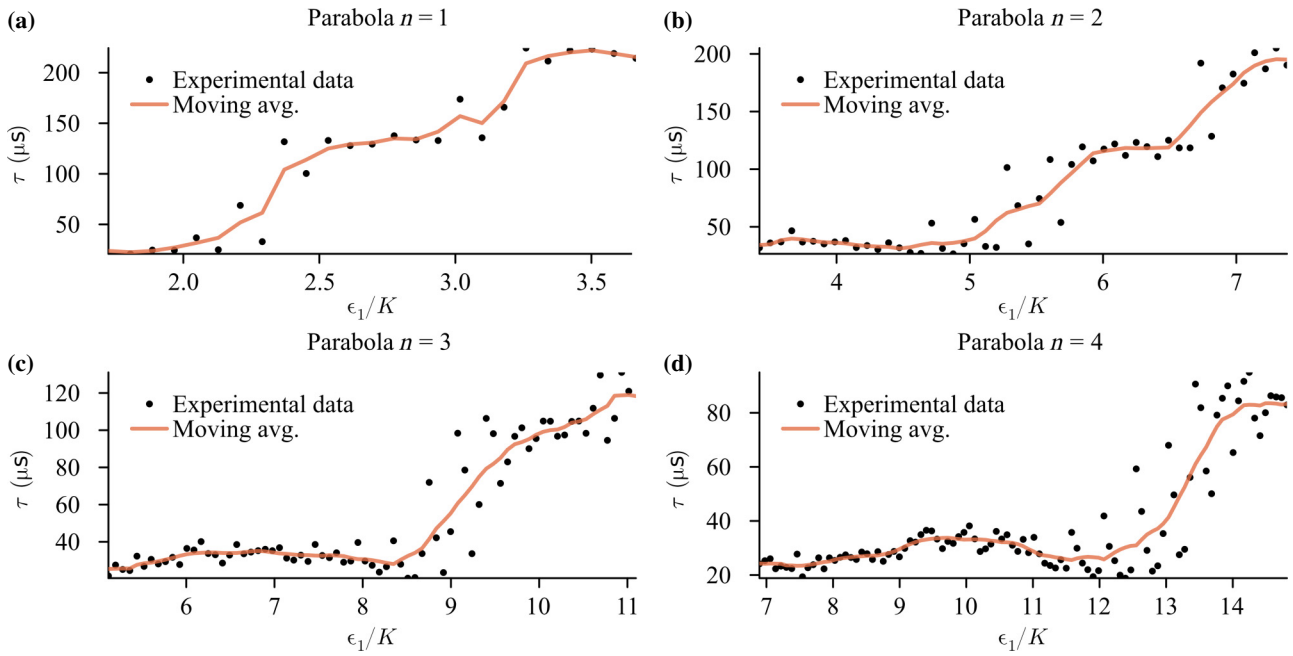

FIG. 16. Experimental lifetimes of Fig. 4(a) along each resonance parabola as parameterized by ϵ_1/K. (a)–(d) show the four parabolas for $n = 1, 2, 3, 4$ as defined by resonance condition Eq. (4). The orange curves are guides to the eye (a moving average).

identically captured by a full numerical quantum treatment. For this, we introduce the inverse logarithmic anticross space (ILAS), denoted by $\mathcal{J}$ and defined as

$$\mathcal{J} \doteq \sum_{n=0}^{N_{\text{cff}}} \left| \frac{1}{\log\left(E_{n+1} - E_n\right)} \right|, \tag{D1}$$

where E_n are the eigenenergies of Eq. (2) at a particular ϵ_1/K and ϵ_2/K and N_{cff} is a numerical cutoff. We plotted a $\mathcal{J}$ color-map as a function of ϵ_1/K and ϵ_2/K, along with two different cuts in Fig. 18.

By construction, $\mathcal{J}$ diverges when a new pair of levels in $\{E_0, E_1, \ldots, E_{N_{\text{cff}}}\}$ are closing. To see this, consider the scenario where the gap between the pair E_0 and E_1 and the gap between the pair E_2 and E_3 are closed, and the rest of the levels are not anticrossing. In this situation, $\mathcal{J}$ is finite, since $\left|(1/(\log\left(E_{n+1} - E_n\right)))\right|$ is zero for the two closed pairs and finite for $E_2 - E_1$ and the rest of the levels (which are distant from one another). Consider now levels E_4 and E_5 interacting, starting to close their gap as in Fig. 2(d). These interacting levels will close and at some point have an energy difference $E_4 - E_5 = 1$ where $\left|(1/(\log\left(E_{n+1} - E_n\right)))\right|$ will diverge. In this way, $\mathcal{J}$ picks up poles near new anticrossings reproducing Fig. 4 as can be seen in Figs. 18(b) and 18(c) in greater detail. Observe the close agreement between the semiclassical treatment, the resonance condition Eq. (4), and $\mathcal{J}$.

APPENDIX E: EFFECTS BEYOND THE RWA MODEL

In this appendix, we present experimental data taken for $\epsilon_2/K > 14$ where the static effective (RWA) description used fails, qualitatively, to describe the experiment. In Fig. 14(a), we present the coherent state lifetime up to $\epsilon_2/K \approx 19$, for $\epsilon_1 = 0$. The lifetime increases in a steplike fashion, as predicted by the static effective model [30,31] until it starts decreasing. This decrease may be captured by a more elaborated static effective treatment [35]. However, resonant-like drops of the lifetime appear too, which challenge the static effective treatment, even if they can also be captured in principle [58]. Time-dependent Floquet simulation of the driven system (not shown, see Ref. [23]) suggest that these resonances may be explained by a single-mode treatment of the nonlinear transmon oscillator. Below, we present and discuss control experiments supporting the viewpoint that these effects belong to the nonlinear physics of single-mode driven systems.

As a control experiment to learn more about these resonances, we measure their temporal stability by repeating the same measurement again after 24 h [see orange and blue graphs in Fig. 14(a)]. This provides important information since the parameters of spurious two-level-systems (TLS) [62–64] coupled to transmons are known to fluctuate in this timescale, and TLS are a plausible candidate for this resonant-like lifetime drops at strong drives. We recalibrated the qubit frequency and observed good agreement between the two measurements, with the resonances being located at the same positions. This data suggests that

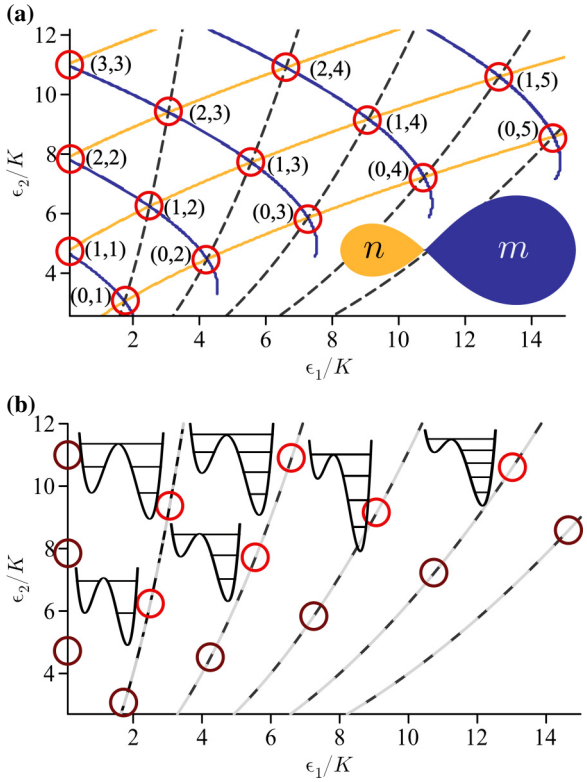

FIG. 17. Semiclassical and Hamiltonian description of Fig. 4(a). (a) Reproduction of Fig. 4(c) with red circles highlighting the incoming resonant levels. (b) Same as (a) with cartoon double-well potentials of Eq. (2) with H_{eff}'s eigenenergies drawn in the well corresponding to the location of its eigenstate. Note the resonance between left and right eigenstates and that the new incoming levels are near the top of the barrier marking the start of a new step in τ. Double-wells corresponding to dark red circles are not shown.

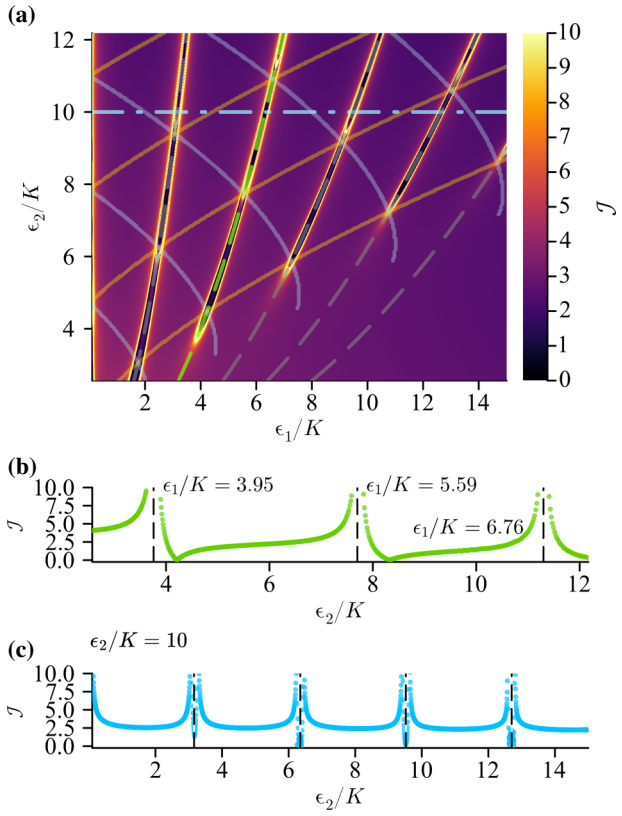

FIG. 18. Numerical quantum treatment and analysis. (a) Heatmap of $\mathcal{J}$ (numerical quantum treatment) with the semiclassical prediction on top [see Fig. 4(c)]. (b) Plot of $\mathcal{J}$ along the green dashed line in (a) parameterized by ϵ_2/K. Vertical black dashed lines indicate the location of the singularities of $\mathcal{J}$ which happen very close to the triple blue-orange intersections. (c) Plot of $\mathcal{J}$ along the horizontal blue dashed line at $\epsilon_2/K = 10$ in (a) parameterized by ϵ_1/K. Vertical black dashed lines indicate the resonance condition from Eq. (4). The different semiclassical predictions agree well with the full quantum Hamiltonian calculation.

the resonances are stable in time and are therefore likely associated with stable electromagnetic transitions and not fluctuating TLSs.

Next, we study these resonances as a function of the detuning $\Delta = (\omega_2/2) - \omega_a$ between the squeezing drive and the resonance frequency of the SNAIL transmon. The system is initialized in one well and after 24 μs the remaining population is measured. This is a proxy for the coherent states' lifetime and thus resonances manifest themselves as a low remaining population. Figure 14(b) depicts this lifetime proxy as a function of detuning and photon number. This data contains resonances moving in different directions. Other features can be seen, for example, around $\epsilon_2/K = 15$ and $\Delta/K = -2$: here two resonances cross (i.e., no avoided crossing), which could provide a bound to the possible coupling between the involved modes. Lastly, we point out a feature around $\epsilon_2/K = 19$ and $\Delta/K = 2$, where one of the resonances seems to split up into two.

Moving beyond the case of $\epsilon_1 = 0$, we now study the impact of an additional drive on the resonances. In Fig. 11(a), we show the equienergy contours of the effective Hamiltonian for $\epsilon_1 \neq 0$ and $\phi = 0$, which creates an asymmetry between the two wells [see also Fig. 2(c)]. This picture is valid under the RWA, and we have observed its conspicuous failure for $\epsilon_2/K \gg 1$. In Fig. 11(b), for $\epsilon_2/K = 20$ we observe a "forest" of resonances, very different from the case of smaller ϵ_2/K (see Fig. 3). These resonances are not explained by resonant tunneling in the RWA potential and described by Eq. (4), but are instead reminiscent to the onset of chaotic behavior [23,65,66]. Changing the photon number [see Fig. 11(c)] leads to a change in the forest of resonances. Similar resonances have been observed during the readout of transmon qubits. Here a possible explanation is that the AC Stark shift, induced by the strong readout drive, tunes the qubit into resonance with lossy modes like TLS [60,61,67]. To test this hypothesis, we change the phase ϕ of our strong linear drive.

For $\phi = 90°$, the RWA double-well stays symmetric [Fig. 11(d)]. In Fig. 11(e), we show the same measurement as in Fig. 11(b) (the same value of ϵ_1), but with a different relative phase between the drives. The absence of resonances in Fig. 11(e) suggests that the effect is beyond a Stark shift into lossy modes. This phase dependence of the spurious resonances has not been observed before. Finally, Fig. 11(f) shows an extended data set (compared to Fig. 4), where the breakdown of the RWA description is self-evident for $\epsilon_2/K > 14$.

While these spurious resonances have not been reported before, the discrepancy in between static-effective open quantum system description of our strongly driven nonlinear system and experimental observations is common to all parametric oscillator experiments in the quantum regime reported in the literature [17,18,25,26,28,68,69]. We believe this discrepancy runs deep into our understanding of quantum physics [34] and is intimately related to the problem of the quantum to classical transition and quantum chaos [65]. We also believe it can be avoided once it is understood, by means as simple as filtering the lines at the relevant frequencies, for example.

Our data set, presenting resonances at different locations in parameter space and of different widths, as well as their dependence on the parametric drive frequency, the parametric drive amplitude, the linear drive amplitude, the relative phase between the linear drive and the parametric drive, and their stability over a period of 24 h, will guide research and lead to better theoretical tools to understand and design parametric processes. We also expect that this data will unlock new tools and proposals to study nonlinear driven quantum systems and quantum chaos in unexplored regimes [66,70–72].

[1] C. S. Wang, J. C. Curtis, B. J. Lester, Y. Zhang, Y. Y. Gao, J. Freeze, V. S. Batista, P. H. Vaccaro, I. L. Chuang, L. Frunzio, L. Jiang, S. Girvin, and R. J. Schoelkopf, Efficient multiphoton sampling of molecular vibronic spectra on a superconducting bosonic processor, Phys. Rev. X **10**, 021060 (2020).

[2] J. Choi, H. Zhou, H. S. Knowles, R. Landig, S. Choi, and M. D. Lukin, Robust dynamic Hamiltonian engineering of many-body spin systems, Phys. Rev. X **10**, 031002 (2020).

[3] J. Sun, L. Cheng, and W. Li, Toward chemical accuracy with shallow quantum circuits: A clifford-based Hamiltonian engineering approach, J. Chem. Theory Comput. **20**, 695 (2024).

[4] N. Lyu, A. Miano, I. Tsioutsios, R. G. Cortiñas, K. Jung, Y. Wang, Z. Hu, E. Geva, S. Kais, and V. S. Batista, Mapping molecular Hamiltonians into Hamiltonians of modular cQED processors, J. Chem. Theory Comput. **19**, 6564 (2023).

[5] L. Guo and V. Peano, Engineering arbitrary Hamiltonians in phase space, Phys. Rev. Lett. **132**, 023602 (2024).

[6] F. Schlawin, M. Gessner, A. Buchleitner, T. Schätz, and S. S. Skourtis, Continuously parametrized quantum simulation of molecular electron-transfer reactions, PRX Quantum **2**, 010314 (2021).

[7] P. W. Anderson, B. I. Halperin, and C. M. Varma, Anomalous low-temperature thermal properties of glasses and spin glasses, Philos. Mag.: J. Theor. Exp. Appl. Phys. **25**, 1 (1972).

[8] W. A. Phillips, Tunneling states in amorphous solids, J. Low Temp. Phys. **7**, 351 (1972).

[9] E. Merzbacher, The early history of quantum tunneling, Phys. Today **55**, 44 (2002).

[10] F. Hund, Zur deutung der molekelspektren. I, Z. Phys. **40**, 742 (1927).

[11] N. Bellonzi, A. Kunitsa, J. T. Cantin, J. A. Campos-Gonzalez-Angulo, M. D. Radin, Y. Zhou, P. D. Johnson, L. A. Martínez-Martínez, M. R. Jangrouei, A. S. Brahmachari, L. Wang, S. Patel, M. Kodrycka, I. Loaiza, R. A. Lang, A. Aspuru-Guzik, A. F. Izmaylov, J. R. Fontalvo, and Y. Cao, Feasibility of accelerating homogeneous catalyst discovery with fault-tolerant quantum computers, arXiv:2406.06335.

[12] G. N. Simm and M. Reiher, Systematic error estimation for chemical reaction energies, J. Chem. Theory Comput. **12**, 2762 (2016).

[13] P. Hänggi, P. Talkner, and M. Borkovec, Reaction-rate theory: Fifty years after Kramers, Rev. Mod. Phys. **62**, 251 (1990).

[14] M. Marthaler and M. I. Dykman, Switching via quantum activation: A parametrically modulated oscillator, Phys. Rev. A **73**, 042108 (2006).

[15] M. I. Dykman, M. Marthaler, and V. Peano, Quantum heating of a parametrically modulated oscillator: Spectral signatures, Phys. Rev. A **83**, 052115 (2011).

[16] D. G. A. Cabral, P. Khazaei, B. C. Allen, P. E. Videla, M. Schäfer, R. G. Cortiñas, A. C. Carrillo de Albornoz, J. Chávez-Carlos, L. F. Santos, E. Geva, and V. S. Batista, A roadmap for simulating chemical dynamics on a parametrically driven bosonic quantum device, J. Phys. Chem. Lett. **15**, 12042 (2024).

[17] A. Grimm, N. E. Frattini, S. Puri, S. O. Mundhada, S. Touzard, M. Mirrahimi, S. M. Girvin, S. Shankar, and M. H. Devoret, Stabilization and operation of a Kerr-cat qubit, Nature **584**, 205 (2020).

[18] N. E. Frattini, R. G. Cortiñas, J. Venkatraman, X. Xiao, Q. Su, C. U. Lei, B. J. Chapman, V. R. Joshi, S. Girvin, R. J. Schoelkopf, S. Puri, and M. H. Devoret, Observation of pairwise level degeneracies and the quantum regime of the arrhenius law in a double-well parametric oscillator, Phys. Rev. X **14**, 031040 (2024).

[19] N. E. Frattini, U. Vool, S. Shankar, A. Narla, K. M. Sliwa, and M. H. Devoret, 3-wave mixing Josephson dipole element, Appl. Phys. Lett. **110**, 222603 (2017).

[20] N. Frattini, Three-wave mixing in superconducting circuits: Stabilizing cats with SNAILs, Dissertation, Yale Graduate School of Arts and Sciences, 2021.

[21] D. Ryvkine and M. I. Dykman, Resonant symmetry lifting in a parametrically modulated oscillator, Phys. Rev. E **74**, 061118 (2006).

[22] D. K. J. Boneß, W. Belzig, and M. I. Dykman, Resonant-force-induced symmetry breaking in a quantum parametric oscillator, Phys. Rev. Res. **6**, 033240 (2024).

[23] I. García-Mata, R. G. Cortiñas, X. Xiao, J. Chávez-Carlos, V. S. Batista, L. F. Santos, and D. A. Wisniacki, Effective versus Floquet theory for the Kerr parametric oscillator, Quantum **8**, 1298 (2024).
[24] M. Marthaler and M. I. Dykman, Quantum interference in the classically forbidden region: A parametric oscillator, Phys. Rev. A **76**, 010102 (2007).
[25] J. Venkatraman, R. G. Cortinas, N. E. Frattini, X. Xiao, and M. H. Devoret, A driven Kerr oscillator with two-fold degeneracies for qubit protection, Proc. Natl. Acad. Sci. U.S.A. **121**, e2311241121 (2024).
[26] D. Iyama, T. Kamiya, S. Fujii, H. Mukai, Y. Zhou, T. Nagase, A. Tomonaga, R. Wang, J.-J. Xue, S. Watabe, S. Kwon, and J.-S. Tsai, Observation and manipulation of quantum interference in a superconducting Kerr parametric oscillator, Nat. Commun. **15**, 86 (2024).
[27] S. Puri, S. Boutin, and A. Blais, Engineering the quantum states of light in a Kerr-nonlinear resonator by two-photon driving, npj Quantum Inf. **3**, 18 (2017).
[28] A. Hajr, B. Qing, K. Wang, G. Koolstra, Z. Pedramrazi, Z. Kang, L. Chen, L. B. Nguyen, C. Jünger, N. Goss, I. Huang, B. Bhandari, N. E. Frattini, S. Puri, J. Dressel, A. N. Jordan, D. I. Santiago, and I. Siddiqi, High-coherence Kerr-cat qubit in 2D architecture, Phys. Rev. X **14**, 041049 (2024).
[29] M. Dykman, *Fluctuating Nonlinear Oscillators: From Nanomechanics to Quantum Superconducting Circuits* (Oxford University Press, Oxford, 2012).
[30] R. Gautier, A. Sarlette, and M. Mirrahimi, Combined dissipative and Hamiltonian confinement of cat qubits, PRX Quantum **3**, 020339 (2022).
[31] H. Putterman, J. Iverson, Q. Xu, L. Jiang, O. Painter, F. G. Brandão, and K. Noh, Stabilizing a bosonic qubit using colored dissipation, Phys. Rev. Lett. **128**, 110502 (2022).
[32] R. G. Cortiñas, Arbitrary nondemolition measurements through Hamiltonian stabilization for quantum error correction, PRX Quantum **6**, 020355 (2025).
[33] Q. Su, R. G. Cortiñas, J. Venkatraman, and S. Puri, Unraveling the switching dynamics in a quantum double-well potential, Phys. Rev. A **112**, 042202 (2025).
[34] A. D. Stone, Einstein's unknown insight and the problem of quantizing chaos, Phys. Today **58**, 37 (2005).
[35] J. Venkatraman, X. Xiao, R. G. Cortiñas, and M. H. Devoret, Nonlinear dissipation in a driven superconducting circuit, Phys. Rev. A **110**, 042411 (2024).
[36] O. Benhayoune-Khadraoui, C. Lledó, and A. Blais, How the Kerr-cat qubit dies-and how to rescue it, arXiv:2507.06160.
[37] A. Z. Ding, B. L. Brock, A. Eickbusch, A. Koottandavida, N. E. Frattini, R. G. Cortiñas, V. R. Joshi, S. J. de Graaf, B. J. Chapman, S. Ganjam, L. Frunzio, R. J. Schoelkopf, and M. H. Devoret, Quantum control of an oscillator with a Kerr-cat qubit, Nat. Commun. **16**, 5279 (2025).
[38] F. Adinolfi, D. Z. Haxell, A. Bruno, L. Michaud, V. H. Kamrul, P. Pandey, and A. Grimm, Enhancing Kerr-cat qubit coherence with controlled dissipation, arXiv:2511.01027.
[39] J. M. Jean, R. A. Friesner, and G. R. Fleming, Application of a multilevel Redfield theory to electron transfer in condensed phases, J. Chem. Phys. **96**, 5827 (1992).
[40] A. Ishizaki and G. R. Fleming, On the adequacy of the Redfield equation and related approaches to the study of quantum dynamics in electronic energy transfer, J. Chem. Phys. **130**, 234110 (2009).
[41] N. P. Vu, D. Dong, X. Dan, N. Lyu, V. Batista, and Y. Liu, A computational framework for simulations of dissipative nonadiabatic dynamics on hybrid oscillator-qubit quantum devices, J. Chem. Theory Comput. **21**, 6258 (2025).
[42] V. So, M. Duraisamy Suganthi, A. Menon, M. Zhu, R. Zhuravel, H. Pu, P. G. Wolynes, J. N. Onuchic, and G. Pagano, Trapped-ion quantum simulation of electron transfer models with tunable dissipation, Sci. Adv. **10**, eads8011 (2024).
[43] C. Sias, A. Zenesini, H. Lignier, S. Wimberger, D. Ciampini, O. Morsch, and E. Arimondo, Resonantly enhanced tunneling of bose-einstein condensates in periodic potentials, Phys. Rev. Lett. **98**, 120403 (2007).
[44] M. H. Devoret, J. M. Martinis, D. Esteve, and J. Clarke, Resonant activation from the zero-voltage state of a current-biased Josephson junction, Phys. Rev. Lett. **53**, 1260 (1984).
[45] Y. Yu, D. Nakada, J. C. Lee, B. Singh, D. S. Crankshaw, T. P. Orlando, K. K. Berggren, and W. D. Oliver, Energy relaxation time between macroscopic quantum levels in a superconducting persistent-current qubit, Phys. Rev. Lett. **92**, 117904 (2004).
[46] Z. Dutton, K. V. R. M. Murali, W. D. Oliver, and T. P. Orlando, Electromagnetically induced transparency in superconducting quantum circuits: Effects of decoherence, tunneling, and multilevel crosstalk, Phys. Rev. B **73**, 104516 (2006).
[47] Y. Yu, W. D. Oliver, J. C. Lee, K. K. Berggren, L. S. Levitov, and T. P. Orlando, Multi-photon, multi-level dynamics in a superconducting persistent-current qubit, arXiv:cond-mat/0508587.
[48] D. H. Slichter, R. Vijay, S. J. Weber, S. Boutin, M. Boissonneault, J. M. Gambetta, A. Blais, and I. Siddiqi, Measurement-induced qubit state mixing in circuit QED from up-converted dephasing noise, Phys. Rev. Lett. **109**, 153601 (2012).
[49] M. Schaefer, R. Cortinas, N. Frattini, Q. Su, S. Puri, and M. Devoret, in *Bulletin of the American Physical Society*, Vol. 2024 (American Physical Society, College Park, MD, 2024), p. Q47.010.
[50] J. R. Friedman, Quantum tunneling and classical barrier reduction for a mesoscopic spin, Phys. Rev. B **57**, 10291 (1998).
[51] D. Hoshi, T. Nagase, S. Kwon, D. Iyama, T. Kamiya, S. Fujii, H. Mukai, S. Ahmed, A. F. Kockum, S. Watabe, F. Yoshihara, and J.-S. Tsai, Entangling Schrödinger's cat states by bridging discrete- and continuous-variable encoding, Nat. Commun. **16**, 1309 (2025).
[52] IBM Quantum, The IBM Quantum roadmap, IBM Quantum Computing Blog (2023), https://www.ibm.com/quantum/blog/quantum-roadmap-2033.
[53] M. I. Dykman and V. N. Smelyanskiy, Quantum theory of transitions between stable states of a nonlinear oscillator interacting with a medium in a resonant field, Zh. Eksp. Teor. Fiz **94**, 61 (1988).
[54] A. S. Darmawan, B. J. Brown, A. L. Grimsmo, D. K. Tuckett, and S. Puri, Practical quantum error correction with the XZZX code and Kerr-cat qubits, PRX Quantum **2**, 030345 (2021).

[55] Y. Suzuki, S. Kawabata, T. Yamamoto, and S. Masuda, Quantum state tomography for Kerr parametric oscillators, Phys. Rev. Appl. **20**, 034031 (2023).

[56] N. E. Frattini, V. V. Sivak, A. Lingenfelter, S. Shankar, and M. H. Devoret, Optimizing the nonlinearity and dissipation of a SNAIL parametric amplifier for dynamic range, Phys. Rev. Appl. **10**, 054020 (2018).

[57] B. Bhandari, I. Huang, A. Hajr, K. Yanik, B. Qing, K. Wang, D. I. Santiago, J. Dressel, I. Siddiqi, and A. N. Jordan, Symmetrically threaded SQUIDs as next generation Kerr-cat qubits, PRX Quantum **6**, 030338 (2025).

[58] X. Xiao, J. Venkatraman, R. G. Cortiñas, S. Chowdhury, and M. H. Devoret, Diagrammatic method to compute the effective Hamiltonian of a driven nonlinear oscillator, Phys. Rev. Appl. **24**, 044021 (2025).

[59] M. F. Dumas, B. Groleau-Paré, A. McDonald, M. H. Muñoz-Arias, C. Lledó, B. D'Anjou, and A. Blais, Measurement-Induced Transmon Ionization, Phys. Rev. X **14**, 041023 (2024).

[60] T. Thorbeck, Z. Xiao, A. Kamal, and L. C. G. Govia, Readout-induced suppression and enhancement of superconducting qubit lifetimes, Phys. Rev. Lett. **132**, 090602 (2024).

[61] V. V. Sivak, A. Eickbusch, B. Royer, S. Singh, I. Tsioutsios, S. Ganjam, A. Miano, B. L. Brock, A. Z. Ding, L. Frunzio, S. M. Girvin, R. J. Schoelkopf, and M. H. Devoret, Real-time quantum error correction beyond break-even, Nature **616**, 50 (2023).

[62] P. Klimov *et al.*, Fluctuations of energy-relaxation times in superconducting qubits, Phys. Rev. Lett. **121**, 090502 (2018).

[63] M. Chen, J. C. Owens, H. Putterman, M. Schäfer, and O. Painter, Phonon engineering of atomic-scale defects in superconducting quantum circuits, Sci. Adv. **10**, eado6240 (2024).

[64] T. Thorbeck, A. Eddins, I. Lauer, D. T. McClure, and M. Carroll, Two-level-system dynamics in a superconducting qubit due to background ionizing radiation, PRX Quantum **4**, 020356 (2023).

[65] J. Chávez-Carlos, M. A. Prado Reynoso, R. G. Cortiñas, I. García-Mata, V. S. Batista, F. Pérez-Bernal, D. A. Wisniacki, and L. F. Santos, Driving superconducting qubits into chaos, Quantum Sci. Technol. **10**, 015039 (2024).

[66] I. García-Mata, M. A. P. Reynoso, R. G. Cortiñas, J. Chávez-Carlos, V. S. Batista, L. F. Santos, and D. A. Wisniacki, Impact of chaos on the excited-state quantum phase transition of the Kerr parametric oscillator, Phys. Rev. A **111**, L031502 (2025).

[67] D. Sank *et al.*, Measurement-induced state transitions in a superconducting qubit: Beyond the rotating wave approximation, Phys. Rev. Lett. **117**, 190503 (2016).

[68] Z. Wang, M. Pechal, E. A. Wollack, P. Arrangoiz-Arriola, M. Gao, N. R. Lee, and A. H. Safavi-Naeini, Quantum dynamics of a few-photon parametric oscillator, Phys. Rev. X **9**, 021049 (2019).

[69] A. Yamaguchi, S. Masuda, Y. Matsuzaki, T. Yamaji, T. Satoh, A. Morioka, Y. Kawakami, Y. Igarashi, M. Shirane, and T. Yamamoto, Spectroscopy of flux-driven Kerr parametric oscillators by reflection coefficient measurement, New J. Phys. **26**, 043019 (2024).

[70] S. Habib, K. Shizume, and W. H. Zurek, Decoherence, chaos, and the correspondence principle, Phys. Rev. Lett. **80**, 4361 (1998).

[71] W. H. Zurek and J. P. Paz, Decoherence, chaos, and the second law, Phys. Rev. Lett. **72**, 2508 (1994).

[72] W. H. Zurek and J. P. Paz, in *Epistemological and Experimental Perspectives on Quantum Physics*, edited by D. Greenberger, W.L. Reiter, and A. Zeilinger (Springer Science+Business Media, Dordrecht, 1999), p. 167.